Accepted Manuscript

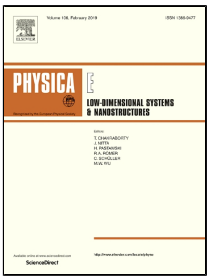

Oxygen-vacancy-related Giant permittivity and Ethanol sensing response in $SrTiO_{3-\delta}$ ceramics

H. Trabelsi, M. Bejar, E. Dhahri, M.A. Valente, M.P.F. Graça

PII:	S1386-9477(18)30936-6
DOI:	10.1016/j.physe.2018.12.025
Reference:	PHYSE 13413
To appear in:	*Physica E: Low-dimensional Systems and Nanostructures*
Received Date:	25 June 2018
Accepted Date:	21 December 2018

Please cite this article as: H. Trabelsi, M. Bejar, E. Dhahri, M.A. Valente, M.P.F. Graça, Oxygen-vacancy-related Giant permittivity and Ethanol sensing response in $SrTiO_{3-\delta}$ ceramics, *Physica E: Low-dimensional Systems and Nanostructures* (2018), doi: 10.1016/j.physe.2018.12.025

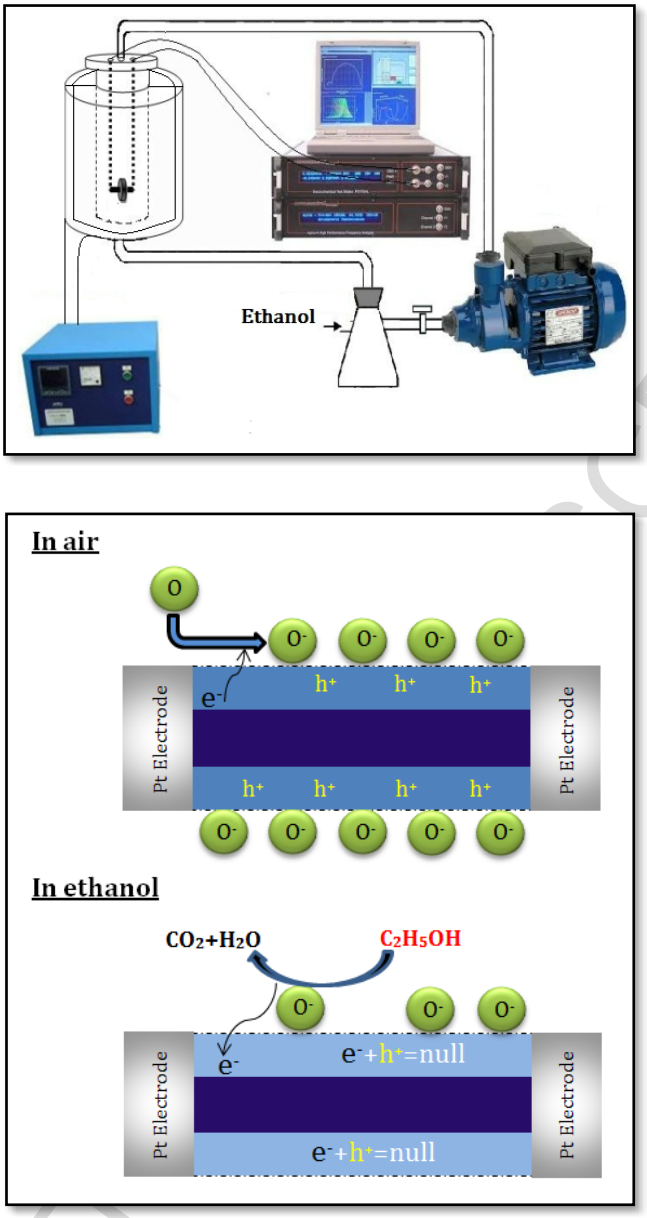

Figure: Gas sensing measurement system & The schematic diagram of the proposed gas-sensing mechanism for *p*-type semiconducting sensor: In air and in ethanol gas.

Oxygen-vacancy-related Giant permittivity and Ethanol sensing response in $SrTiO_{3-\delta}$ ceramics

H. Trabelsi[a,*], M. Bejar[a], E. Dhahri[a], M.A. Valente[b], M.P.F. Graça[b]

[a] Laboratoire de Physique Appliquée, Faculté des Sciences, B.P. 1171, 3000 Sfax, Université de Sfax, Tunisie

[b] I3N and Physics Department, University of Aveiro, 3810-193 Aveiro, Portugal

Abstract

The ethanol sensing properties of $SrTiO_{3-\delta}$ (δ=0.075 and 0.125) ceramics was analyzed by dielectric measurements. The ceramics were prepared by solid state reaction method followed by the creation of oxygen vacancies-δ, through a thermal activated process. The crystal symmetry, space group and unit cell dimensions were derived from the X-ray diffraction (XRD) data using FullProf software whereas grain's size distribution was assessed by scanning electron microscopy (SEM). The prepared samples have been analyzed by impedance spectroscopy over the frequency range from 100 Hz to 1 MHz and temperature range from 240 to 340 K. The dielectric properties of $SrTiO_{3-\delta}$ ceramics showed a quite remarkable stability of giant permittivity (> 10^4) as well as a low dielectric loss, which open ways for several applications such as over voltage protections of electronic devices. A low-frequency dielectric relaxation behavior was found, and the carriers for electrical conduction result from the first-ionization of oxygen vacancies. The conductivity and gas sensitivity of $SrTiO_{3-\delta}$-based sensors were investigated. Results demonstrated that the conductivity decreases after the introduction of the ethanol gas, and *p*-type semiconductor gas-sensing materials were obtained. Both characteristics present higher responses at lower optimal operating temperatures.

Keywords: $SrTiO_3$; Oxygen vacancy; Giant permittivity; Gas-sensor.

*** Corresponding author:** ***trabelsi.hamdi@rocketmail.com***

1. Introduction

Stoichiometric $SrTiO_3$ (STO) is a well-known metal oxide with a cubic perovskite structure above 105 K (lattice parameter $a_C = 3{,}905$ Å). Below this temperature it undergoes a structural transition to a tetragonal phase ($a_T = b_T = a_C\sqrt{2}$ and $c_T = 2a_C$). Many investigations on STO ceramic have been carried out to obtain high permittivity and a low dielectric loss, including STO-based grain boundary barrier layer capacitors [1], $Sr_{1-x}Ba_xTiO_3$ ceramics [2] and Bi^{3+} doped STO ceramics [3], whose dielectric properties are due to the interfacial effects, ferroelectric phases and ionization of oxygen vacancies, respectively. The colossal permittivity is most probably caused by the Schottky barrier in grain boundary. Recently, the colossal dielectric properties of based titanium materials have been investigated. Ga^{3+} co-doped TiO_2 ceramic can exhibit high permittivity value of 10^5 at 1 kHz [4].

Moreover, the STO is a semiconducting oxide sensing material that has been well studied for oxygen sensor. It shows oxygen sensing properties in both *p*- and *n*-type semiconductor states. As *p*-type oxygen sensors, Fe-doped STO [5] and Mg-doped [6] have been reported and as a *n*-type sensor, STO without dopant [7] has been reported. It was found that the resistivity increases and decreases with decreasing the oxygen partial pressure in *p*-type semiconductor and in *n*-type semiconductor, respectively.

Oxygen vacancies in STO are known to dope the material with electron carriers, which cause superconductivity [8], and metallic nature [9], as well as switchable resistive states [10] depending on the extent of doping. Deliberate variation of oxygen content allows one to modify this material not only from an *n*-type conductor to *p*-type, but also from an electronic to an ionic conductor. According to the global charge equilibrium, Ti^{4+} in STO can be transformed into Ti^{3+} when oxygen vacancies are created and the precise chemical formula of the STO may be written as:

$$Sr^{2+}Ti^{4+}_{1-2\delta}Ti^{3+}_{2\delta}O^{2-}_{3-\delta} \qquad \textbf{Eq. (1)}$$

where δ corresponds to the loss of oxygen from the stoïchiometric compound. The role of oxygen vacancies (V_0) and their related defects are often the proposed culprits in various reliability limiting processes of oxide perovskite materials. The V_0 is doubly charged with respect to the neutral lattice and is considered to be the most mobile intrinsic ionic defect in these materials. It is considered that oxygen vacancies act as donors in STO, as follows:

$$V_0 \Leftrightarrow V_0^{\bullet} + e^{-} \quad \text{Eq. (2)}$$

$$V_0^{\bullet} \Leftrightarrow V_0^{\bullet\bullet} + e^{-} \quad \text{Eq. (3)}$$

where $V_0^{\bullet}$ is the first-ionization of oxygen vacancies, $V_0^{\bullet\bullet}$ the second-ionization of oxygen vacancies, and e^{-} an electron. Below room temperature, the oxygen-vacancy-related relaxation usually behaves as a polaronic relaxation due to electron hopping (generated by the ionization of oxygen vacancies) between polyvalent ions [11]. Whereas in the temperature region above room temperature, the oxygen-vacancy-related relaxation processes can be produced by single-ionized, doubly-ionized, and diffusion of oxygen vacancies as well as the oxygen vacancy complexes composed of oxygen and other cation vacancies [12, 13].

Based on these considerations the purpose of the present work is to study the dielectric properties of the oxygen-vacancies $SrTiO_{3-\delta}$ compounds. Moreover, the sensing mechanism of $SrTiO_{3-\delta}$ ceramics has also been investigated based on some designed experiments.

2. Experimental details

The STO parent compound was prepared using the conventional solid state reaction method. Highly pure powders of $SrCO_3$ and TiO_2 (having a purity of more than 99.9% for each of them) were mixed in an agate mortar in the desired proportion according to the following equation:

$$SrCO_3 + TiO_2 \rightarrow SrTiO_3 + CO_2 \quad \text{Eq. (4)}$$

The resulting ground mixture was calcined at 800 °C for 12 hours in order to remove the unreacted carbon compounds and the organic material. The obtained powder was pressed into disc-pellet forms (of about 2 *mm* thickness and 5 *mm* diameter) and sintered at 1100 °C for 2 days and then to 1300 °C for the same duration under oxygen atmosphere with several periods of grinding and repelling. These cycles of pressing, annealing and grinding were performed to ensure that the reaction took place and to improve homogeneity and crystallinity. Finally, these pellets were cooled slowly to room temperature in air. As our parent compound has been synthesized under oxygen atmosphere, it is consequently stoichiometric in oxygen.

In order to create the oxygen vacancies, the parent compound was put into a quartz-tube containing a portion of Ti in the metallic state, which absorbs oxygen as it is described in the following equation reaction:

$$SrTiO_3 + \frac{\delta}{2}Ti(metal) \rightarrow SrTiO_{3-\delta} + \frac{\delta}{2}TiO_2 \qquad \textbf{Eq. (5)}$$

with δ = 0.075 and 0.125.

Afterwards, the quartz tube was annealed at 800 °C as described in reference [14]. At such temperature, Ti (metal) removed oxygen from perovskite phase to get the desired $SrTiO_{3-\delta}$ compositions. The supposed nominations of the prepared samples are: STO1 (δ=0.075) and STO2 (δ=0.125). To monitor the reaction, the obtained products were weighted by using an ultra-micro balance and the level of the created oxygen vacancies was checked according to the following equation:

$$\delta = \frac{\Delta m \times M_{mol}}{m_{used} \times M_0} \qquad \textbf{Eq. (6)}$$

With:

Δm : Mass difference of the compound before and after the reaction;

M_{mol} : Molar mass of the stoïchiometric $SrTiO_3$ compound;

m_{used} : Weight of the used $SrTiO_3$ compound;

M_0 : Atomic mass of oxygen;

The determined δ values are in good agreement with the desired one with an error of 10^{-4}. Furthermore, it was reported that the presence of V_0 in STO material can be confirmed by electron paramagnetic resonance (EPR) measurement [15-17]. In our previous work, we have already controlled the amount of the paramagnetic V_0 by employing the EPR measurement and the signal intensity was found to increase from STO1 to STO2, supporting the hypothesis that the V_0 concentration in $SrTiO_{3-\delta}$ samples increases with the δ-rate [17].

The crystalline phase of the synthesized $SrTiO_{3-\delta}$ samples was confirmed by XRD analysis using a Siemens D5000 X-ray diffractometer, with monochromator Cu-Kα radiation (λ_{Cu}= 1.540598 Å), at room temperature. The data was collected in the 2θ range of 20° ≤ 2θ ≤ 90° with a step scanning of 0.02° and a counting time of 5 s per step. Surface morphological features of the obtained samples were analyzed by Zeiss 1530 scanning electron microscope.

Impedance spectroscopy measurements ($Z^* = Z' - jZ''$) were performed as a function of the temperature and frequency, between 240 – 340 K and 100 Hz – 1 MHz, respectively. The complex impedance was measured using an Agilent 4294A impedance analyzer, in the C_p-R_p configuration. Since the samples have a disk shape, with a considerably larger diameter relatively to their thickness, platinum electrodes were used to measure the electrical transport across the compound and the capacitance in a plate capacitor configuration. The complex permittivity can be calculated through the measured complex impedance by applying **Eqs. (7)** and **(8) [18]**:

$$\varepsilon' = \frac{d}{A}\frac{C_p}{\varepsilon_0} \qquad \textbf{Eq. (7)}$$

$$\varepsilon'' = \frac{d}{A}\frac{1}{\omega R_p \varepsilon_0} \qquad \textbf{Eq. (8)}$$

where ε' is the real part of the complex permittivity, commonly referred as dielectric constant, ε'' is the imaginary part of the complex permittivity, also known as the loss factor, C_p and R_p are the parallel capacitance and resistance, respectively, d and A are the sample thickness and electrode area, ω is the angular frequency and ε_0 is the vacuum permittivity (8.8542×10^{-12} F/*m*).

From the complex permittivity values, the complex modulus can be calculated, which is defined as the inverse of the complex permittivity, being the real and imaginary parts given by **Eq. (9)** and **(10)**, respectively **[19]**:

$$M' = \frac{\varepsilon'}{\varepsilon'^2 + \varepsilon''^2} \qquad \textbf{Eq. (9)}$$

$$M'' = \frac{\varepsilon''}{\varepsilon'^2 + \varepsilon''^2} \qquad \textbf{Eq. (10)}$$

To investigate the ethanol sensing properties of $SrTiO_{3-\delta}$ compounds, the samples were introduced in a test chamber formed by a vertical electric furnace and a dry rotary pump, in a closed loop setup, connected to the extremes of the furnace. The latter operates from room temperature up to 1473 K. When the resistance of the sensors was stable, a specific amount of the ethanol vapor was injected into the chamber through an inlet port. Desired concentration of ethanol gas was calculated using the following formula:

$$C(\text{ppm}) = \frac{22.4\times\rho\times d\times V_1}{M\times V_2} \qquad \textbf{Eq. (11)}$$

where ρ (g/mL) is the density of the liquid, d is the purity of the liquid, V_1 (L) is the volume of the liquid, V_2 (L) is the volume of the test chamber, and M (g/mol) is the molecular weight of the liquid.

At this stage, the electrical resistance of the sensors was measured continuously between 330 and 640 K in the presence of 100 *ppm* ethanol gas and the gas response (Sensitivity) was evaluated by the following equation:

$$\text{Sensitivity} = \frac{R_{gas} - R_{air}}{R_{air}} \qquad \textbf{Eq. (12)}$$

where R_{air} is the resistance of sensor measured in air and R_{gas} is the resistance of sensors measured in the test gas equipment. **Fig. 1** shows the schematic diagram of the experimental sensor setup.

We conclude this section by recalling that we made ceramic thick disc-pellets with 2 *mm* thickness and 5 *mm* diameter with smooth surface, so that we can apply high voltages, and to avoid the formation of micro-cracks, which develop with thermal cycling during the electrical measurements. Indeed, plane capacitor configuration was used for all of the studies and the cylindrical pellets were pressed between platinum electrodes while avoiding short-circuiting the leads and to ensure the high gas adsorption at the surface area of the solid in an automated manner.

3. Results and discussion

The XRD diffractograms, obtained at room temperature, of the STO1 and STO2 samples are presented in **Fig. 2**. Both results indicate that each monophasic sample crystallizes in the cubic structure with the *Pm-3m* space group. XRD Rietveld refinements were carried out with a *Pm-3m* space group at room temperature by using FullProf program **[20]**, and no systematic variation of the lattice parameter is observed. Based on the Scherrer's equation **[21]**: $D_{XRD} = 0.89\lambda / FWHM \times \cos\theta$ (in which λ is the X-ray wavelength in nanometer, θ is ½ the diffraction angle and FWHM is the full width half maximum in radian), the calculated average crystallite sizes D_{XRD} were 146.437 and 149.229 *nm* for STO1 and STO2, respectively. It must be pointed out that the grain size calculations from XRD are just estimations. To guarantee accurate results on the size distributions, it is important to ensure that the diffraction data are of high resolution. Obviously, the accuracy depends on uncertainties of peak position, its full width half maximum

(FWHM) value and the applied Scherrer constant. In order to improve our accuracy in this way, samples have been scanned slowly (by increasing counting time and decreasing step size) which may help as to improve the quality of the peak profile fit. And of course we chose an appropriate value of the Scherrer constant which can be taken as 0.89 for integrated breadth of spherical crystal with cubic unit cell. To gain optimum accuracy it remains to reduce the uncertainty in FWHM as much as possible. Peak broadening arises from two sources: Instrumental contribution and sample contribution. The instrumental broadening is generally obtained while determining particle sizes of the extremely thin or small particles, and it can in fact affect the value of the FWHM. So, this instrumental broadening needs to be eliminated to obtain broadening exclusively due to the sample effect. On the other hand, massive and polycrystalline specimens generally exhibit a line broadening due to the presence of crystallite size effect as well as microstrain effect. In this case, we may need the help of the Williamson-Hall technique (W-H) to separate these factors and to get an error from the quality of the linear fit. The crystallite size (D_{W-H}) and the microstrain ($C\varepsilon$) are calculated using the following relation [22]:

$$\beta_i \cos\theta_i = \frac{0.89\lambda}{D_{W-H}} + 4C\varepsilon \times \sin\theta_i$$

where β_i is the integrated breadth (in radians 2θ) of the *i*th Bragg reflection positioned at $2\theta_i$. By plotting $\beta\cos\theta$ versus $4\sin\theta$, the slope and the ordinate intercept of the W–H plot can be used to quantify the volume-weighted crystallite size and microstrain contributions to peak broadening. **Fig. 3** shows the W–H plots for STO1 and STO2. The six diffraction planes with high intensities [(110), (111), (200), (211), (220) and (310)] indicating the preferential orientation of the microcrystalline were used for the calculation. The estimated values of the crystallite size were found to be 172.721 and 189.505 *nm* for samples STO1 and STO2, respectively. Generally, the source of microstrain is ascribed to crystal imperfections, such as excess volume of grain boundaries, vacancies and vacancy clusters and dislocations. The dislocation density is defined as the length of dislocation lines per unit volume of the crystal, and it is estimated from knowing the crystallite size by the formula [23]: $\varepsilon \approx 1/D^2$ (where ε is the dislocation density). There is a progressive increasing in microstrain and dislocation density with the oxygen vacancies percentage.

The insets of **Fig. 2** are the SEM images of the free surface of STO1 and STO2 samples. They consist of both large and small agglomerated-grains characterized by various shapes with some micro-pores, which is in line with our previous results **[24]**. The estimated average grain sizes are about 0.638 and 1.026 μm for STO1 and STO2, respectively. These values are higher than those of the crystallite sizes determined previously from the Scherer formula as well as the W-H method related to X-ray diffraction patterns.

The frequency dependence of the real part of dielectric permittivity (ε') and loss tangent ($\tan\delta = \varepsilon''/\varepsilon'$) of $SrTiO_{3-\delta}$ samples as a function of temperatures are shown in **Fig. 4** and **5**, respectively. As it can be seen, ε' at low frequency is rather high (above 10^4) and is found to decrease by increasing frequency of the applied field at constant temperature. This behavior can be explained by the fact that, at lower frequency region, the permanent dipoles align themselves along the direction of the field and contribute to the total polarization of the dielectric material. On the other hand, at higher frequency the variation in field is too rapid for the dipoles to align themselves in the direction of field, *i.e.*, dipoles can no longer follow the field, so their contribution to the total polarization and hence to the dielectric permittivity become negligible. Therefore the dielectric constant (ε') decreases with increase in frequency **[25]**. Also, the dielectric constant increased with the increase of temperature, which promotes the mobility and therefore the increase of the loss tangent. Such step-like behavior of dielectric constant looks like the dielectric spectra of giant dielectric constant material such as $CaCu_3Ti_4O_{12}$ **[26]**.

Here, it should be noted that $SrTiO_{3-\delta}$ ceramics show a higher values of dielectric constant and loss tangent compared to the $SrTiO_3$ stoichiometric material **[18]**. At room temperature, they have maximum values of dielectric constant ~15380 and ~12270, for STO1 and STO2, respectively. On the other hand, the minimum values of loss tangent factors are ~0.2 and ~0.4, for STO1 and STO2, respectively. At high frequencies (~1 MHz), for STO2 sample, the dielectric constant becomes almost independent of temperature, which may be due to ionic polarization **[27]**.

It was shown that the ionization of the oxygen vacancies creates conduction electrons which might be bounded to Ti^{4+} leading to the Ti^{3+} formation, according to **Eq. (1)**. A Ti^{3+} can be viewed as a Ti^{4+} that traps an electron ($Ti^{4+} \bullet e$) which means that the [$Ti^{4+} \bullet e - V^{\bullet\bullet} - Ti^{4+} \bullet e$] bonds are formed. Under this condition, electrons will be bound

by the fully ionized oxygen vacancies. Then giant defect-dipoles are produced, which result in a giant permittivity and a low dielectric loss. These electrons may easily become conducting electrons by thermal activation and the dielectric behavior will be dependent on the ionization of oxygen vacancies, leading to large temperature and frequency-dependent dielectric properties [28].

For STO2 sample, the dielectric loss relaxation peak, which is centered in the dispersion region of ε', is detected at lower frequency compared with STO1 sample. It appears and corresponds to the dielectric constant relaxation in the frequency range of 10^3–10^6 Hz. Also, this peak becomes broader and shifts to higher frequency with increasing temperature, showing a thermally activated process. These results suggest that the dielectric relaxation becomes easily produced in more oxygen vacancies introduced.

Complex modulus analysis is a well-established method for interpreting the dynamical aspects of electrical transport phenomena (*i.e.* parameters such as carrier/ion hopping rate, conductivity relaxation time, etc…). The complex electric modulus spectrum M'' versus M' is shown in Fig. 6 for STO1 and STO2 samples at different temperatures. The patterns are characterized by the presence of little asymmetric and depressed semicircular arcs whose centre does not lie on M' axis. The behavior of electric modulus spectrum is suggestive of the temperature dependent hopping type of mechanism for electric conduction in the system and non-Debye type dielectric relaxation.

Fig. 7 shows the variation of the real part of the electric modulus M' as a function of frequency at various temperatures. It was observed that the M' value is very low (approaching zero) in the low frequency region. This behavior can be interpreted by a lack of restoring force which governs the mobility of charge carriers under the influence of an electric field [29]. Otherwise, an increase in the value of M' with increasing frequency at different temperatures has been observed.

In Fig. 8 are displayed the variation of imaginary part M'' with frequency at different temperatures. From Fig. 8, two peaks are apparent, representing the response of grain boundary and bulk regions. The high-frequency M'' peak may correspond to semiconducting core (grain) and the smaller low-frequency peak is caused by interfacial or grain boundary effect. From the above consideration, it may be said that, grain boundary resistance dominates the overall impedance for $SrTiO_{3-\delta}$ samples. Besides, it can be observed that the frequency values corresponding to the low-frequency peak shift to higher frequencies. The broadening of this peak suggests the spread of relaxation

time with different time constants, which indicates that is non-exponential and this profile approves the non-Debye relaxation. The relaxation time (τ) is determined using the relation, $2\pi f_{max}\tau = 1$, where f_{max} is the frequency corresponding to the peak of M'' spectra. The relaxation time may be explained by a thermally activated transport of Arrhenius type governed by the relation:

$$\tau = \tau_0 \exp(E_a / k_B T) \qquad \textbf{Eq. (13)}$$

where τ_0 is the pre-exponential factor, E_a is the activation energy, k_B the Boltzmann constant ($k_B = 8.618 \times 10^{-5}\ eV\ K^{-1}$) and T the temperature.

The slopes of the linear fits yield the thermal activation energy and the values of activation energy were found to be 0.103 and 0.092 *eV* for STO1 and STO2, respectively. For both samples, activation energy lower than 0.2 *eV* may be assigned to the first ionization energy of an oxygen vacancy **[30]**. Depending on the V_0 migration rate inside STO ceramic, activation energies larger than 0.2 *eV* are related to $V_0^{\bullet\bullet}$, while the electron require lower activation energy to hop via single oxygen vacancies ($V_0^{\bullet}$) **[31]**. On the basis of these results, it can be suggested that in the temperature range between 240 and 340 K, the free conduction electrons result from the $V_0^{\bullet}$ as described in **Eq. (2)**. Furthermore, the activation energy in the $SrTiO_{3-\delta}$ samples decreases with increasing oxygen vacancy content. In fact, with the increase in V_0 concentration, the correlation among the OVs strengthens and thus the movement of V_0 becomes easier and the activation energy decreases **[32]**. Small activation energy was also observed in the Mn-doped STO ceramic, which was considered to be due to the structural cubic-to-tetragonal antiferrodistortive phase transition at low temperature **[33]**.

To further ponder the manner of the confined carriers, the imaginary component of impedance (Z'') and modulus (M'') as a function of frequencies at selected temperatures (*i.e.* 240, 270, 310 and 340 K) are plotted in **Fig. 9**. It is reported that in the combined Z'' and M'' plots, if the M'' peak coincide with Z'' peak at the same frequency, the conduction mechanism is dominated by the long range movement of charge carriers. If the peak of M'' versus frequency does not coincide with Z'' peak the relaxation process is dominated by short range movement of charge carriers. The figures display the slight mismatch between M'' and Z'' peaks of the samples at the whole range of temperature. The hopping of carriers under external electrical field acts as the

reorientation of dipoles. Therefore, it is proposed that in the present samples, the carriers are localized and the relaxation process is dominated by short range movement of charge carriers, suggesting the departure from ideal Debye-type behavior. However, in accordance with our calculated activation energies, we can also conclude that the carriers (generated by the ionization of oxygen vacancies) are confined to potential wells, being mobile over short distances.

To study the effect of the ethanol gas on the resistance of $SrTiO_{3-\delta}$ sensors, impedance spectroscopy is also measured when the sensors are exposed to the ethanol gas at the temperature range between 330 and 640 K. The temperature dependences of the conductivity in air and during target gas exposure are shown in **Fig. 10**. It is noted that the conductivity was increased with increasing temperature due to an intrinsic characteristic of a semiconductor. This would result from the ionization of oxygen vacancies with the increasing of working temperature. We also found that the conductivities in ethanol are smaller than those in air, accompanying positive response. This means that $SrTiO_{3-\delta}$ samples are *p*-type semiconducting materials and their charge carriers are dominated by holes.

The principle of gas detection for semiconducting metal oxides mainly involves the gas adsorption, charge transfer, and desorption process. It is based on the resistance variation of the sensing element, which depends on the gas atmosphere and on the operating temperature of the sensing material exposed to the test gas. The detailed conduction model of *p*-type oxide semiconductors is well explained by Barsan et al. **[34]**. The model is introduced to explain the sensing mechanism in scheme **Fig. 11**. $SrTiO_{3-\delta}$ ceramics interact with the oxygen, by transferring the electrons from the valence band to adsorbed oxygen atoms, forming ionic species such as O_2^- or O^-. At high temperatures (above 373 K), the O^- species is more dominated than any other oxygen adsorbate. Oxygen adsorption process can be described by the following reactions **[35]**:

$$O_{2(gas)} \leftrightarrow O_{2(ads)} \qquad \textbf{Eq. (14)}$$

$$O_{2(ads)} + e^- \leftrightarrow O^-_{2(ads)} \qquad \textbf{Eq. (15)}$$

$$O^-_{2(ads)} + e^- \leftrightarrow 2O^-_{(ads)} \qquad \textbf{Eq. (16)}$$

$$O^-_{(ads)} + e^- \leftrightarrow O^{2-}_{(ads)} \qquad \textbf{Eq. (17)}$$

For the *p*-type semiconductor, this electron transferring from the valence band to the chemisorbed oxygen results in a change the electric surface's charge status of the sensor.

It means that an underlying positive accumulation zone formed by holes, inducing a lower resistance layer that covers the entire surface of the gas sensor. Thus, the conduction can be explained by the parallel competition between the conductive hole accumulation layer and the resistive core.

Correspondingly, accompanied with this charge transfer, the formation of a depletion layer will increase the potential barrier near the surface. Furthermore, a larger quantity of oxygen vacancies induces higher adsorptions of oxygen without lowering the expansion level of the depletion layer, which results in a further increase of the conductivity of the STO2-based sensor (δ=0.125). In fact, oxygen vacancies react with the atmospheric oxygen to generate more holes and then make the sample more conductive [36].

$$0.5(O_2)_{gas} + V_0^{\bullet\bullet} \leftrightarrow O_0^{\times} + 2h^{\bullet} \qquad \text{Eq. (18)}$$

where $V_0^{\bullet\bullet}$, $O_0^{\times}$, $h^{\bullet}$ represent oxygen vacancy, lattice oxygen and hole, respectively.

When the sensor is exposed to ethanol, this latter reacts with the chemisorbed oxygen, releasing electrons back to the valence band and results in a recombination of electrons and holes which increases the layer resistance, then the conductivity decreases when the environment changes from air to the ethanol vapor. This chemical processing can be represented by:

$$C_2H_5OH + 6O^{n-} \rightarrow 2CO_2 + 3H_2O + 6ne^- \qquad \text{Eq. (19)}$$

It should give a large number of electrons and a small amount of holes, leading to an increase in the inclusive resistance of the sensor. It is worth noting that the $SrTiO_{3-\delta}$-based sensors will generate a high density of oxygen vacancies when they are exposed to the ethanol gas [17].

The sensitivity of the gas sensor is defined as the capability of the sensor to respond the presence of a given gas concentration. Fig. 12 shows the relationship between the operating temperature and the response to 100 *ppm* of ethanol for as-synthesized $SrTiO_{3-\delta}$. With increasing operating temperature, the response of $SrTiO_{3-\delta}$-sensors increases at first, undergoes a maximum, and finally falls off. Meanwhile, the sensitivity of sensors at each fixed temperature increases with δ-rate and the best sensitivity was obtained around 340 K by the sample with δ=0.125.

With an increase of δ-rate, the gas-response of STO2-based sensor rises rapidly at low temperatures, which implies that this latter has a significantly better sensing

performance than STO1 sensor. This view has been confirmed by the increase of the conductivity with oxygen vacancies concentration, as discussed earlier.

4. Conclusion

In summary, $SrTiO_{3-\delta}$ ceramics with compositions δ=0.075 and 0.125 were prepared by solid state reaction route. XRD confirmed the formation of a single phase crystalline structure. The impedance spectroscopy analysis of $SrTiO_{3-\delta}$ ceramics was done in a frequency ranging from 100 Hz to 1 MHz at different temperatures. A high value of dielectric constant makes our compounds a good candidate for many electronic applications. The observed non-Debye dielectric relaxation, which is related to the oxygen vacancies, followed thermally activated process and the mobile charge carriers in this temperature range are from the first ionization of oxygen vacancies. Besides, the electrical sensing measurements demonstrated that the $SrTiO_{3-\delta}$ sensors are *p*-type semiconductor gas-sensing materials. There is an increase of gas response at lower operating temperature, suggesting that oxygen vacancy plays dominant role for enhancing ethanol sensing properties.

REFERENCES

[1] R. Wernicke, Two-layer model explaining the properties of $SrTiO_3$ boundary layer capacitors, in: L.M. Levinson, D.C. Hill (Eds.), Advances in ceramics, American Ceramic Society, Columbus. (1981) 272–281.

[2] T. Wu, Y. Pu, P. Gao, D. Liu, Influence of Sr/Ba ratio on the energy storage properties and dielectric relaxation behaviors of strontium barium titanate ceramics, J. Mater. Sci: Mater. Electron. 24 (2013) 4105–4112.

[3] Y. Zhi, A. Chen, R.Y. Guo, A.S. Bhalla, L.E. Cross, Oxygen vacancy related dielectric relaxation in $(Sr_{1-1.5x}Bi_x)TiO_3$, Ferroelectrics. 262 (2001) 1193–1199.

[4] W. Tuichai, N. Thongyong, S. Danwittayakul, N. Chanlek, P. Srepusharawoot, P. Thongbai, S. Maensiri, Very low dielectric loss and giant dielectric response with excellent temperature stability of Ga^{3+} and Ta^{5+} co-doped rutile-TiO_2 ceramics, Mater. Des. 123 (2017) 15 –23.

[5] S.J. Litzelman, A. Rothschild, H.L. Tuller, The electrical properties and stability of $SrTi_{0.65}Fe_{0.35}O_{3-\delta}$ thin films for automotive oxygen sensor applications, Sens. Actuators, B, 108 (2005) 231-237.

[6] T. Ding, W. Jia, Electrophoretic deposition of $SrTi_{1-x}Mg_xO_{3-\delta}$ films in oxygen sensor, Sens. Actuators, B, 82 (2002) 284-286.

[7] T. Hara, T. Ishiguro, N. Wakiya, K. Shinozaki, Oxygen sensing properties of $SrTiO_3$ thin films, Jpn. J. Appl. Phys. 47 (2008) 7486-7489.

[8] C.S. Koonce, M.L. Cohen, J.F. Schooley, W.R. Hosler, E.R. Pfeiffer, Superconducting Transition Temperatures of Semiconducting $SrTiO_3$, Phys. Rev. 163 (1967) 380-390.

[9] D.D. Sarma, S.R. Barman, H. Kajueter, G. Kotliar, Spectral functions in doped transition metal oxides, Europhys. Lett. 36 (1996) 307-312.

[10] K. Szot, W. Speier, G. Bihlmayer, R. Waser, Switching the electrical resistance of individual dislocations in single-crystalline $SrTiO_3$, Nature Mat. 5 (2006) 312-320.

[11] C.C. Wang, C.M. Lei, G.J. Wang, X.H. Sun, T. Li, S.G. Huang, H. Wang, Y.D. Li, Oxygen-vacancy-related dielectric relaxations in $SrTiO_3$ at high temperatures, J. Appl. Phys. 113 (2013) 094103-094111.

[12] N. Zhong, S. Okamura, K. Uchiyama, T. Shiosaki, Single-ionized-oxygen-vacancy-related dielectric relaxation in $Bi_{3.25}La_{0.75}Ti_3O_{12}$ ferroelectric films, Appl. Phys. Lett. 87 (2005) 252901-252903.

[13] Q.Q. Ke, X. J. Lou, Y. Wang, J. Wang, Oxygen-vacancy-related relaxation and scaling behaviors of $Bi_{0.9}La_{0.1}Fe_{0.98}Mg_{0.02}O_3$ ferroelectric thin films, Phys. Rev. B. 82 (2010) 024102-024108.

[14] H. Trabelsi, M. Bejar, E. Dhahri, M. Sajieddine, M.A. Valente, A. Zaoui, Effect of the oxygen deficiencies creation on the suppression of the diamagnetic behavior of $SrTiO_3$ compound, J. Alloys Compd. 680 (2016) 560-564.

[15] G. Zhang, W. Jiang, S. Hua, H. Zhao, L. Zhang, Z. Sun, Constructing bulk defective perovskite $SrTiO_3$ nanocubes for high performance photocatalyst, Nanoscale 8 (2016) 16963–16968.

[16] M. Shang, H. Hu, G. Lu, Y. Bi, Synergistic effects of $SrTiO_3$ nanocubes and Ti^{3+} dual-doping for highly improved photoelectrochemical performance of TiO_2 nanotube arrays under visible light, J. Mater. Chem. A 4 (2016) 5849–5853.

[17] H. Trabelsi, M. Bejar, E. Dhahri, M.P.F. Graça, M.A. Valente, M.J. Soares, N.A. Sobolev, Raman, EPR and ethanol sensing properties of oxygen-Vacancies $SrTiO_{3-\delta}$ compounds, Appl. Surf. Sci. 426 (2017) 386–390.

[18] H. Trabelsi, M. Bejar, E. Dhahri, M.P.F. Graça, M.A. Valente, K. Khirouni, Structure, Raman, dielectric behavior and electrical conduction mechanism of strontium titanate, Physica E Low Dimens Syst Nanostruct. 99 (2018) 75-81.

[19] S. Amrin, V.D. Deshpande, Dielectric relaxation and ac conductivity behavior of carboxyl functionalized multiwalled carbon nanotubes/poly (vinyl alcohol) composites, Physica E Low Dimens Syst Nanostruct. 87 (2017) 317-326.

[20] J. Rodrigues-Carvajal, FULLPROF, a Rietveld refinement and pattern matching analysis program, Laboratoire Leon Brillouin, CEA-CNRS, France, 2000.

[21] S. Gopinath, K. Sivakumar, B. Karthikeyen, C. Ragupathi, R. Sundaram, Structural, morphological, optical and magnetic properties of Co_3O_4 nanoparticles prepared by conventional method, Physica E Low Dimens Syst Nanostruct. 81 (2016) 66-70.

[22] S.G. Pandya, J.P. Corbett, W.M. Jadwisienczak, M.E. Kordesch, Structural characterization and X-ray analysis by Williamson–Hall method for Erbium doped Aluminum Nitride nanoparticles, synthesized using inert gas condensation technique, Physica E Low Dimens Syst Nanostruct. 79 (2016) 98-102.

[23] A. Arunachalam, S. Dhanapandian, C. Manoharan, Effect of Sn doping on the structural, optical and electrical properties of TiO_2 films prepared by spray pyrolysis, Physica E Low Dimens Syst Nanostruct. 76 (2016) 35-46.

[24] H. Trabelsi, M. Bejar, E. Dhahri, M. Sajieddine, K. Khirouni, P.R. Prezas, B.M.G. Melo, M.A. Valente, M.P.F. Graça, Effect of oxygen vacancies on $SrTiO_3$ electrical properties, J Alloys Compd. 723 (2017) 894–903.

[25] R. Dridi, I. Saafi, A. Mhamdi, A. Matri, A. Yumak, M. Haj Lakhdar, A. Amlouk, K. Boubaker, M. Amlouk, Structural, optical and AC conductivity studies on alloy ZnO–Zn_2SnO_4 (ZnO–ZTO) thin films, J Alloys Compd. 634 (2015) 179–186.

[26] J. Li, K. Wu, R. Jia, L. Hou, L. Gao, S. Li, Towards enhanced varistor property and lower dielectric loss of $CaCu_3Ti_4O_{12}$ based ceramics, Mater. Des. 92 (2016) 546 –551.

[27] M.V.M. Rao, S.N. Reddy, A.S. Chary, K. Shahi, Complex impedance analysis of $RbNO_3$ and $RbNO_3$:Al_2O_3 dispersed solid electrolyte systems, Physica B. 364 (2005) 306–310.

[28] Z. Wang, M. Cao, Z. Yao, Q. Zhang, Z. Song, W. Hu, Q. Xu, H. Hao, H. Liu, Z. Yu, Giant permittivity and low dielectric loss of $SrTiO_3$ ceramics sintered in nitrogen atmosphere, J. Eur. Ceram. Soc. 34 (2014) 1755–1760.

[29] M. HajLakhdar , T. Larbi, B. Ouni, M. Amlouk, AC conductivity, dielectric relaxation and modulus behavior of Sb_2S_2O new kermesite alloy for optoelectronic applications, Mater. Sci. Semicond. Process. 40 (2015) 596-601.

[30] C. Ang, Z. Yu, L.E. Cross, Oxygen-vacancy-related low-frequency dielectric relaxation and electrical conduction in Bi: $SrTiO_3$,Phys. Rev. B. 62 (2000) 228–236.

[31] R.E. Stanculescu, C.E. Ciomaga, N. Horchidan, C. Galassi, F.M. Tufescu, L. Mitoseriu, The influence of post-sintering re-oxidation treatment on dielectric response of dense and porous $Ba_{0.70}Sr_{0.30}TiO_3$ ceramics, Ceram. Int. 42 (2016) 527-536.

[32] X. Wang, X. Lu, C. Zhang, X. Wu, W. Cai, S. Peng, H. Bo, Y. Kan, F. Huang, J. Zhu, Oxygen-vacancy-related high-temperature dielectric relaxation in $SrTiO_3$ ceramics, J. Appl. Phys. 107 (2010) 114101–114104.

[33] M. Savinov, V.A. Trepakov, P.P. Syrnikov, V. Zelezny, J. Pokorny, A. Dejneka, L. Jastrabik, P. Galinetto, Dielectric properties of Mn doped $SrTiO_3$, J. Phys. Condens. Matter 20 (2008) 095221-095226.

[34] N. Barsan, U. Weimar, Conduction model of metal oxide gas sensors, J. Electroceram. 7 (2001) 143–167.

[35] S. Zhang, P. Song, Q. Wang, Enhanced acetone sensing performance of an α-Fe_2O_3-In_2O_3 heterostructure nanocomposite sensor, J. Phys. Chem. Solids 120 (2018) 261-270.

[36] G. Dong, H. Fan, H. Tian, J. Fang, Q. Li, Gas-sensing and electrical properties of perovskite structure *p*-type barium-substituted bismuth ferrite, RSC Adv. 5 (2015) 29618-29623.

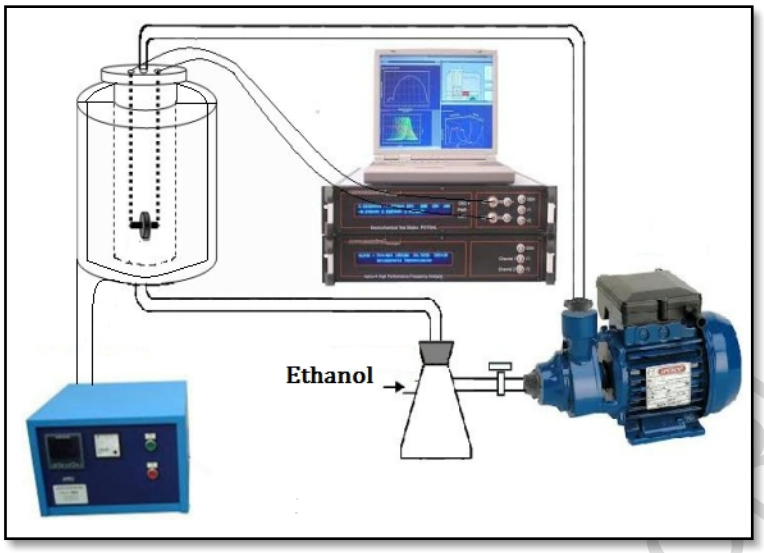

Figure 1: Gas sensing measurement system.

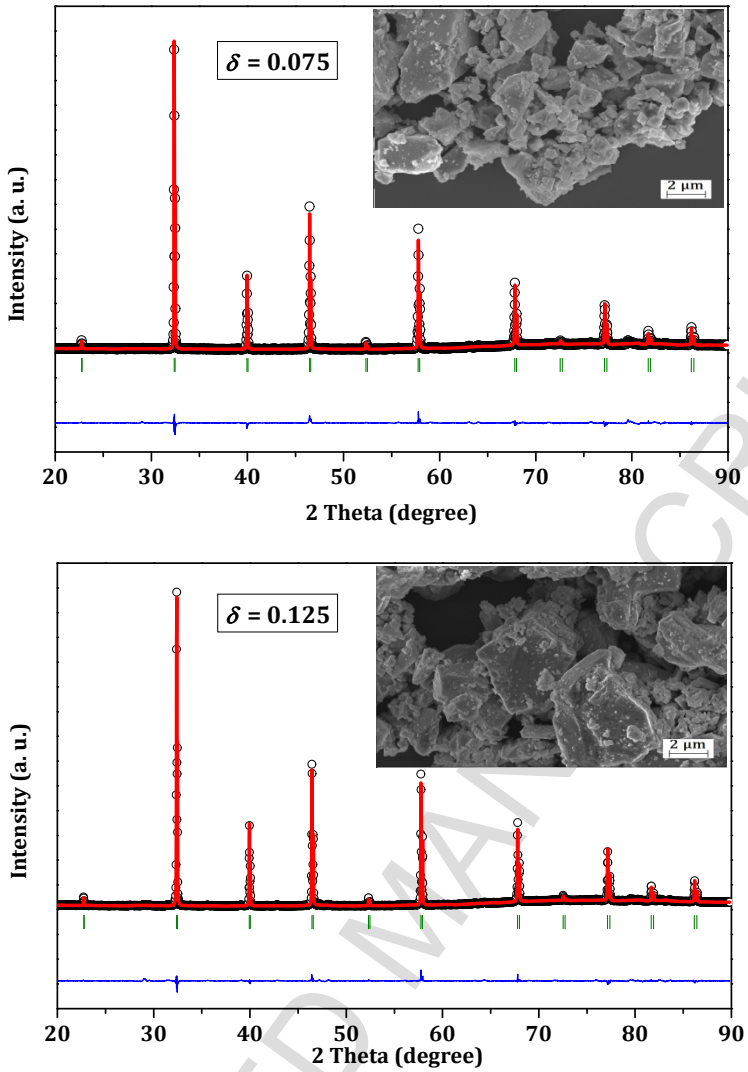

Figure 2: Rietveld refinement of XRD data of $SrTiO_{3-\delta}$ compounds. Solid hollow circle, red line, blue line and green bar mark represent observed, calculated, difference between observed and calculated and Bragg positions respectively. Insets show the SEM images for $SrTiO_{3-\delta}$ (δ= 0.075 and 0.125) samples.

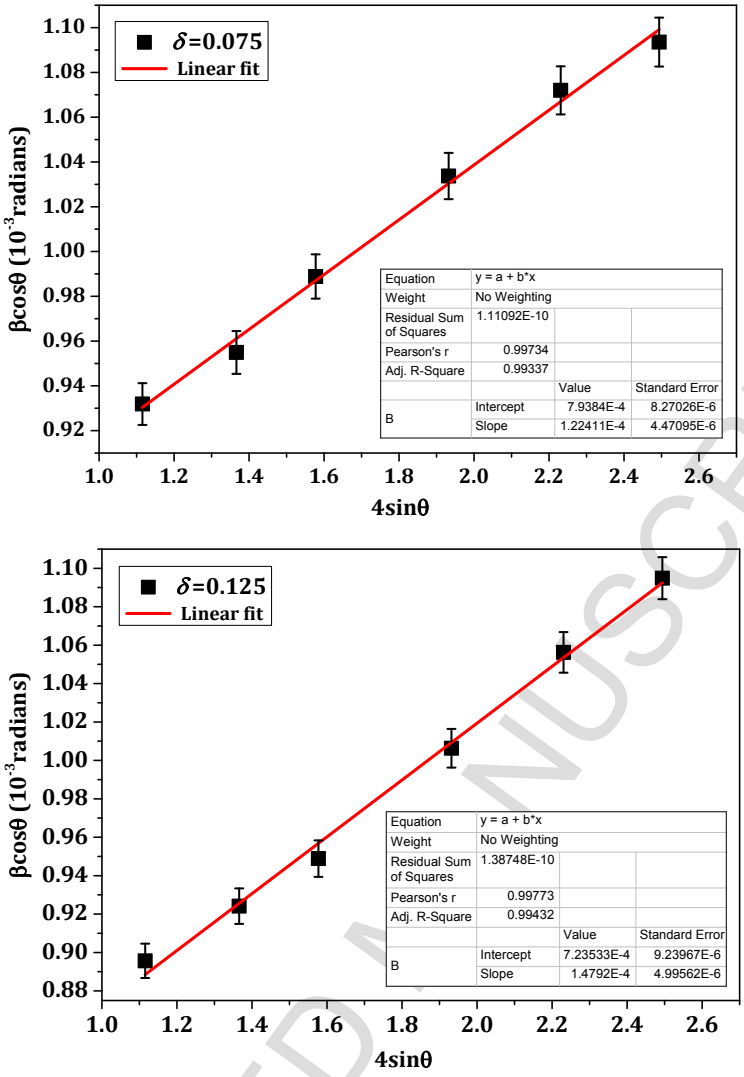

Figure 3: Williamson–Hall plots of $\beta cos\theta$ against $4sin\theta$ for $SrTiO_{3-\delta}$ compounds with linear regression to data.

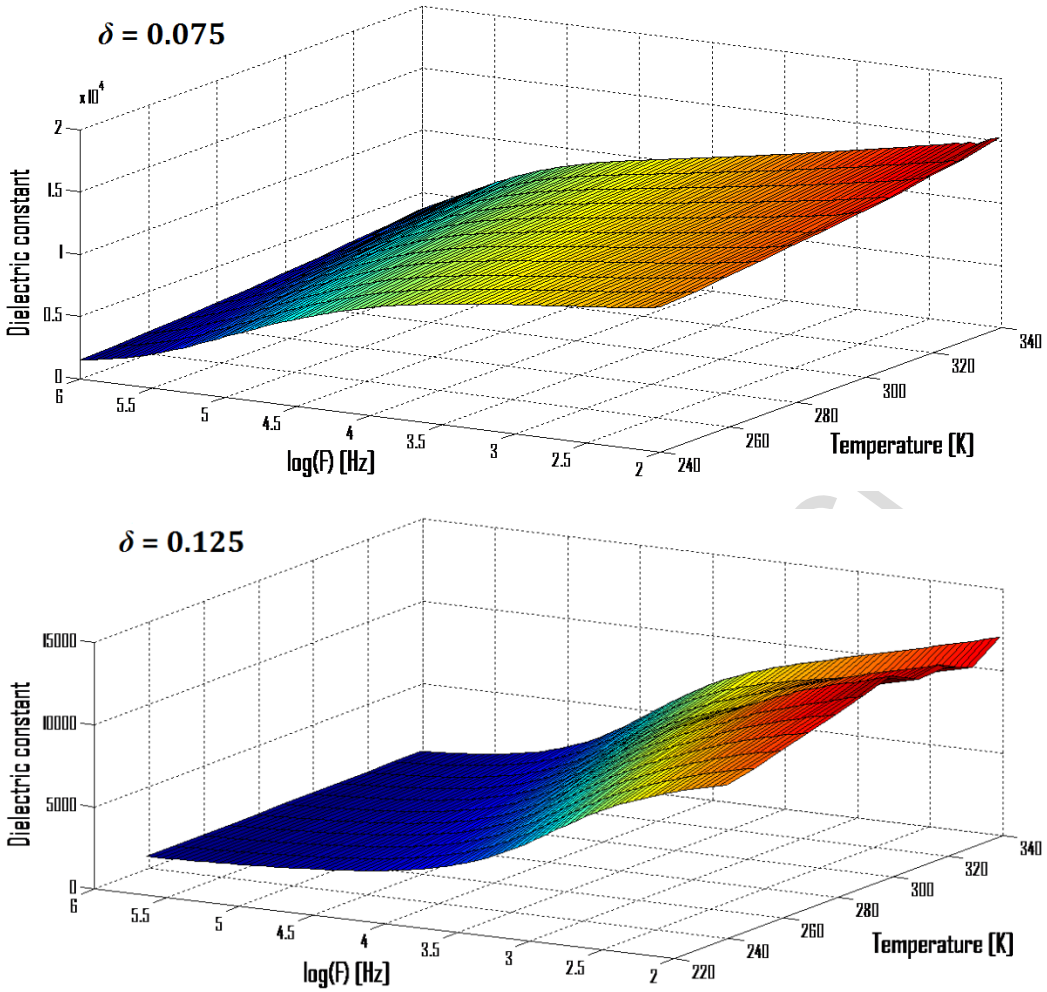

Figure 4: Dependency of the real part of the dielectric constant (ε') of $SrTiO_{3-\delta}$ compounds with the temperature and frequency.

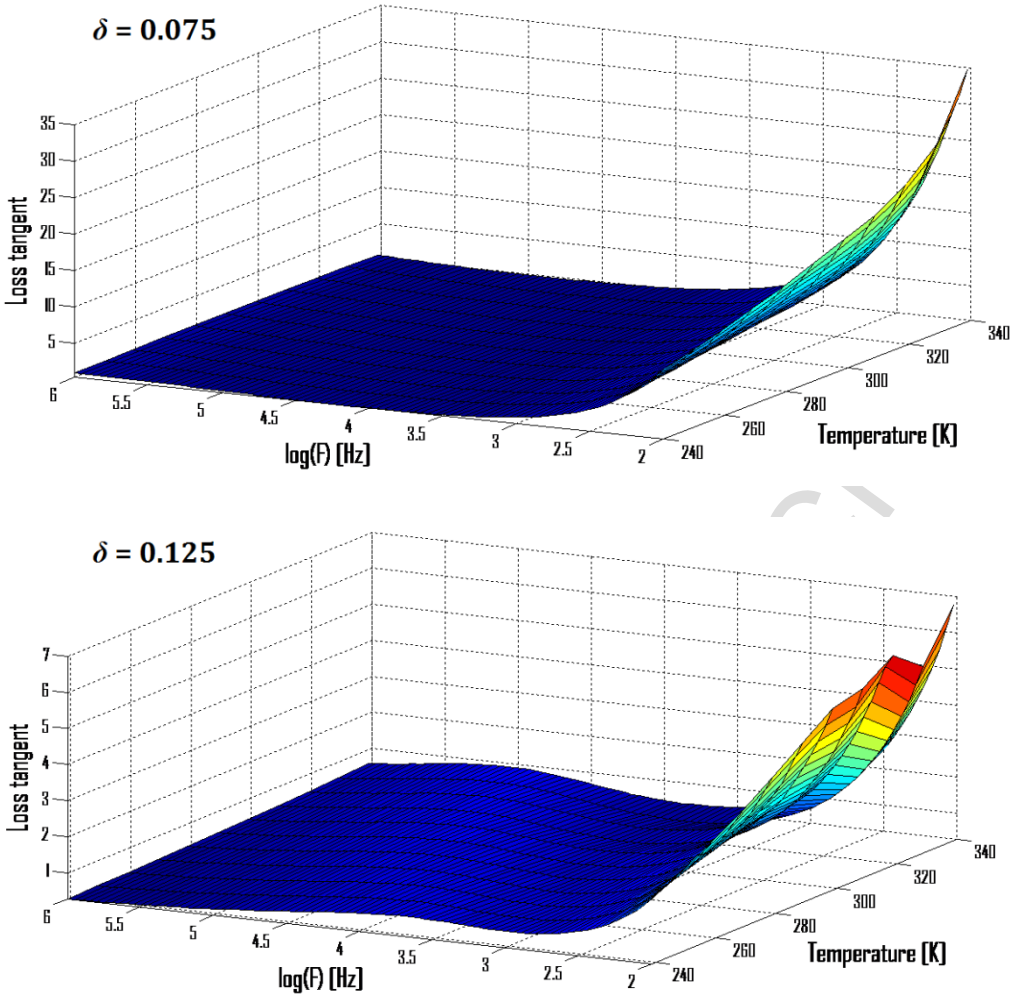

Figure 5: Dependency of the loss tangent ($tan\delta$) of $SrTiO_{3-\delta}$ compounds with the temperature and frequency.

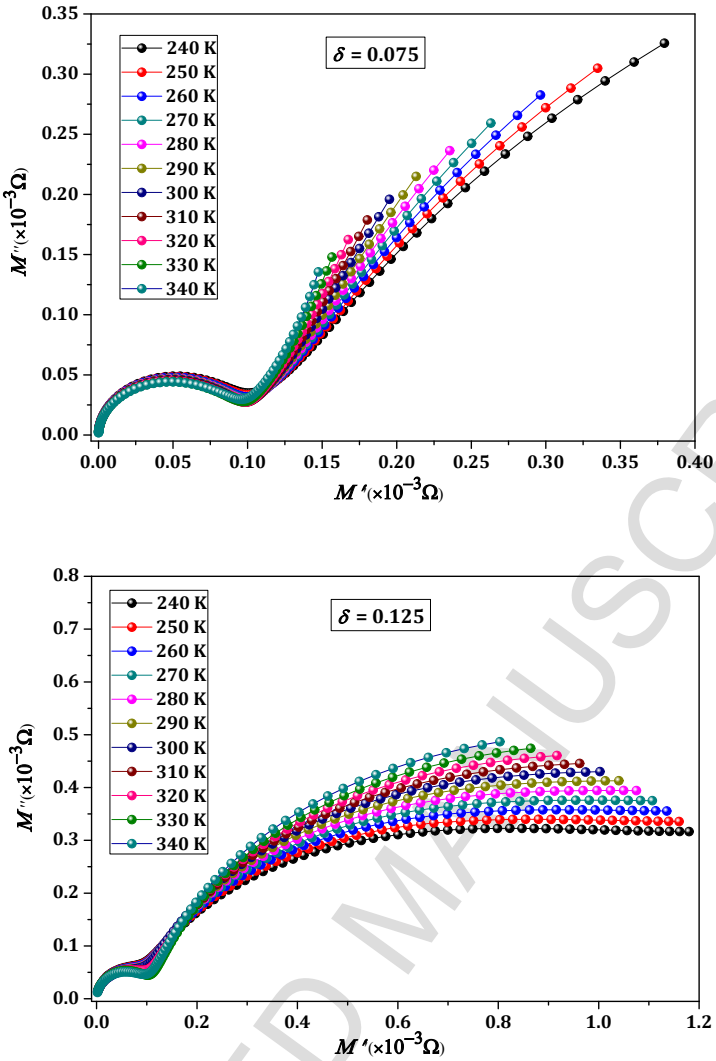

Figure 6: Complex modulus plots of $SrTiO_{3-\delta}$ samples (δ = 0.075 and 0.125) at various temperatures.

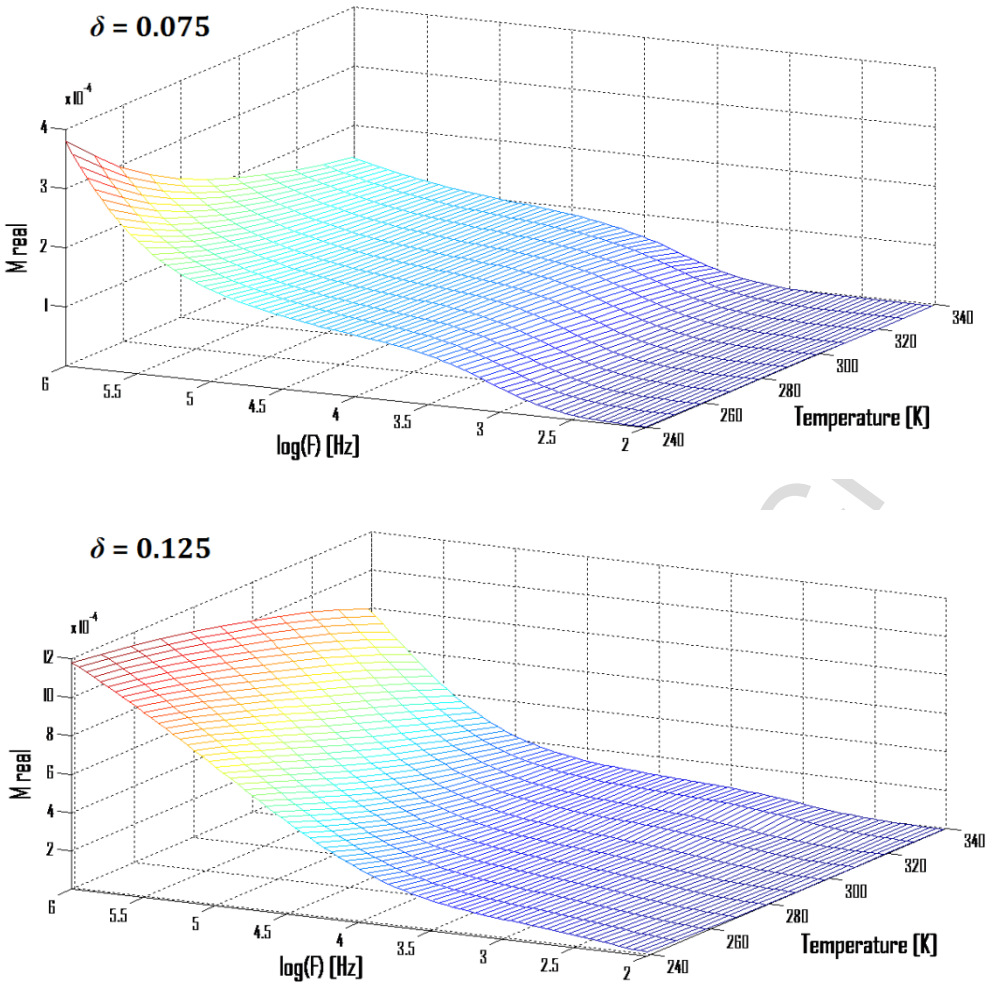

Figure 7: Dependency of the real part of the electric modulus (M') of $SrTiO_{3-\delta}$ compounds with the temperature and frequency.

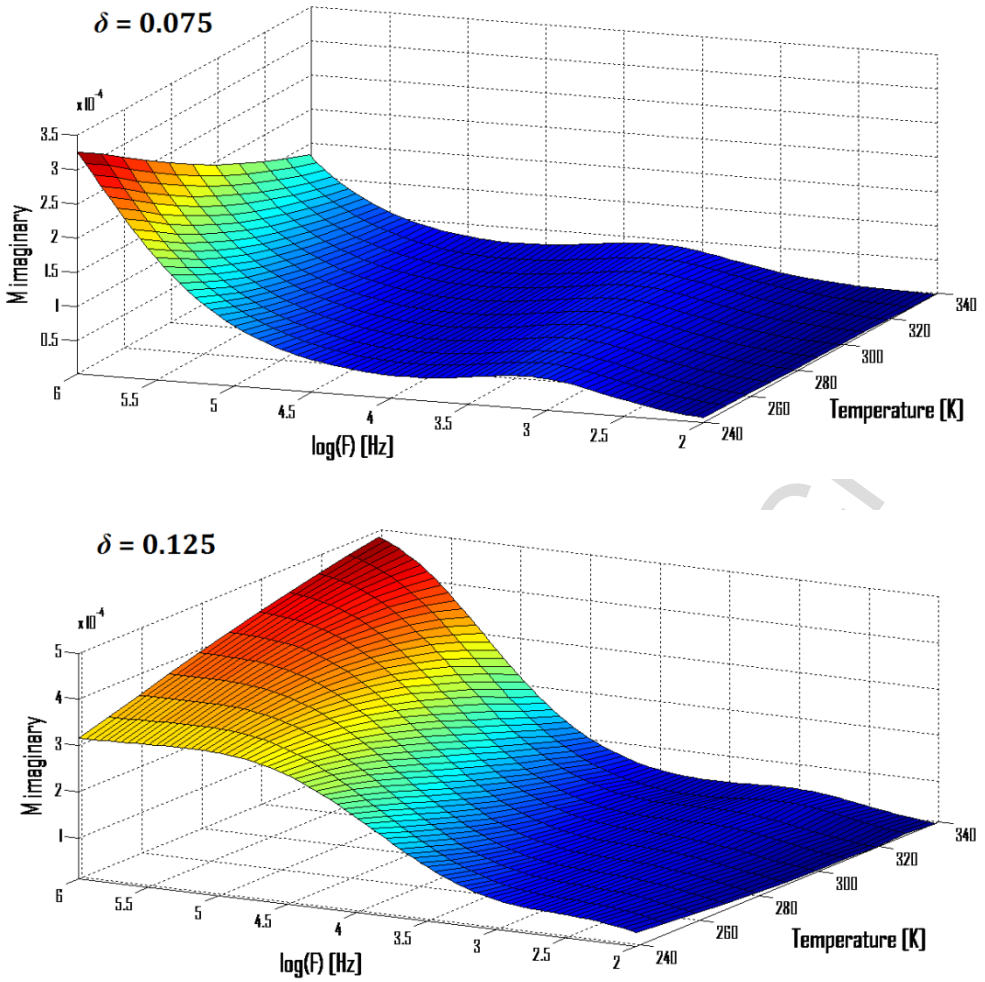

Figure 8: Dependency of the imaginary part of the electric modulus (M'') of $SrTiO_{3-\delta}$ compounds with the temperature and frequency.

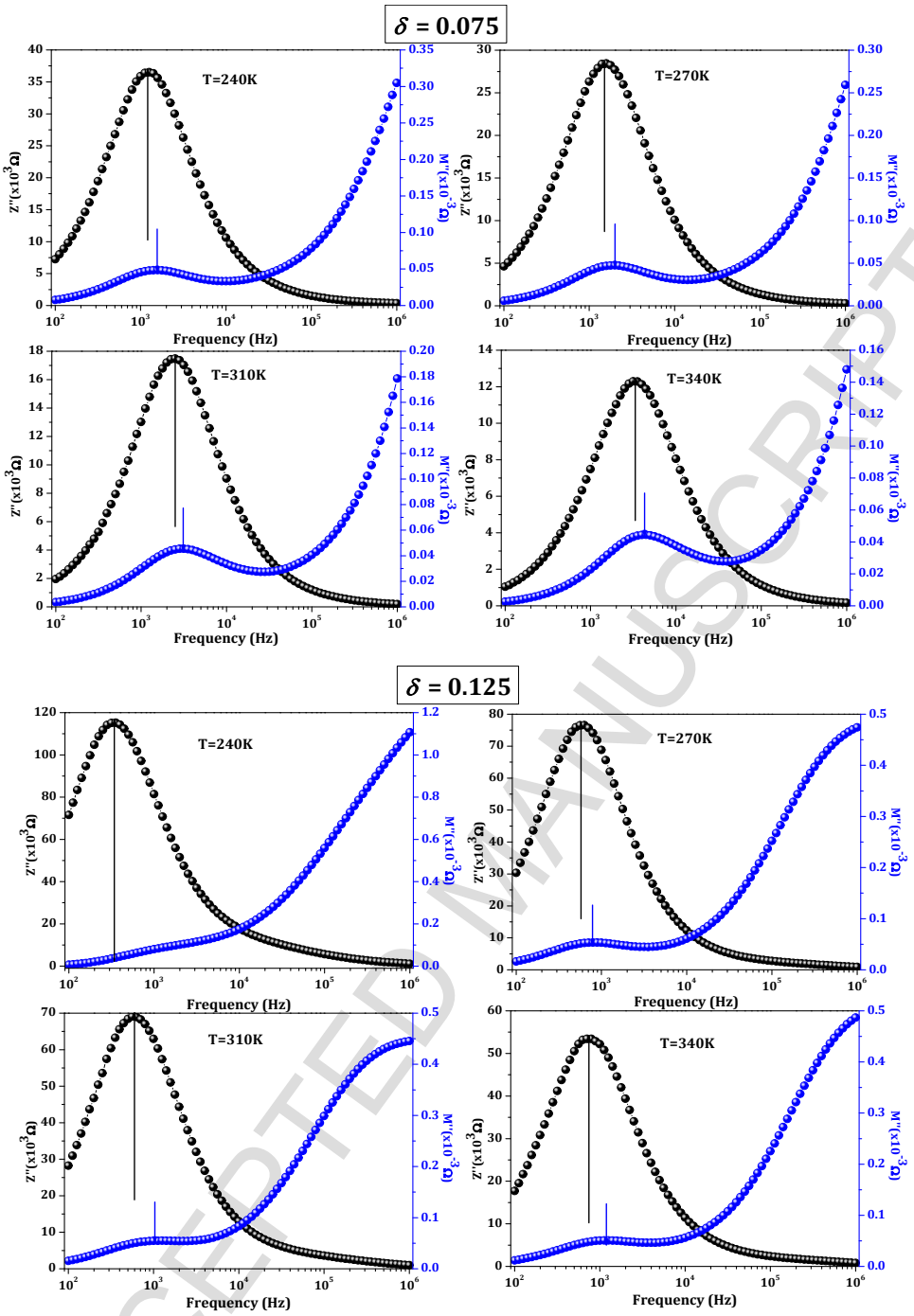

Figure 9: The spectroscopic plots of the impedance (Z'') and electric modulus (M'') at selected temperatures. The vertical lines indicate the peaks in Z'' and M'' curves.

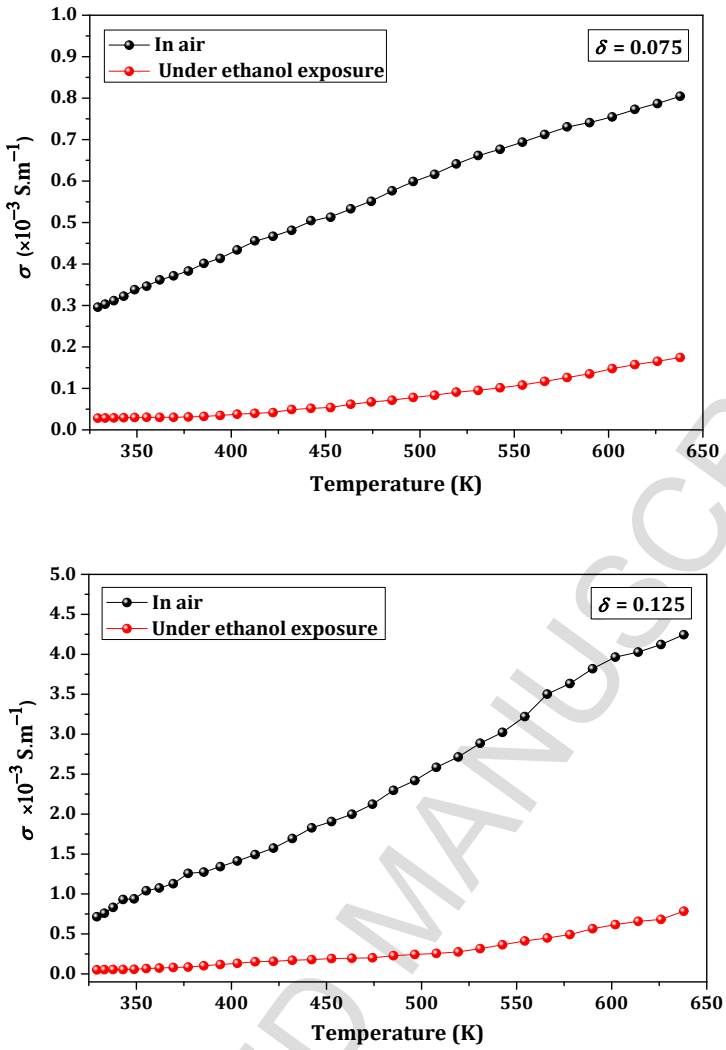

Figure 10: Variation of the conductivity as a function of temperature of $SrTiO_{3-\delta}$ compounds.

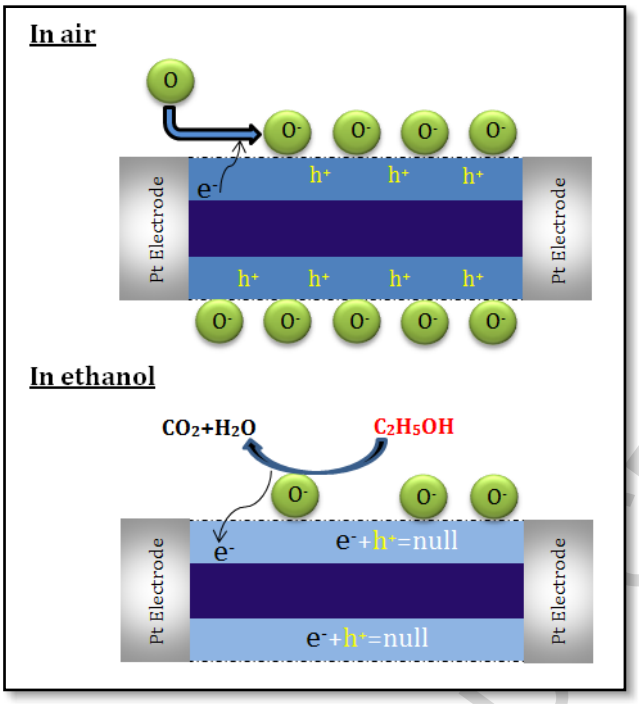

Figure 11: The schematic diagram of the proposed gas-sensing mechanism for *p*-type semiconducting sensor: In air and in ethanol gas.

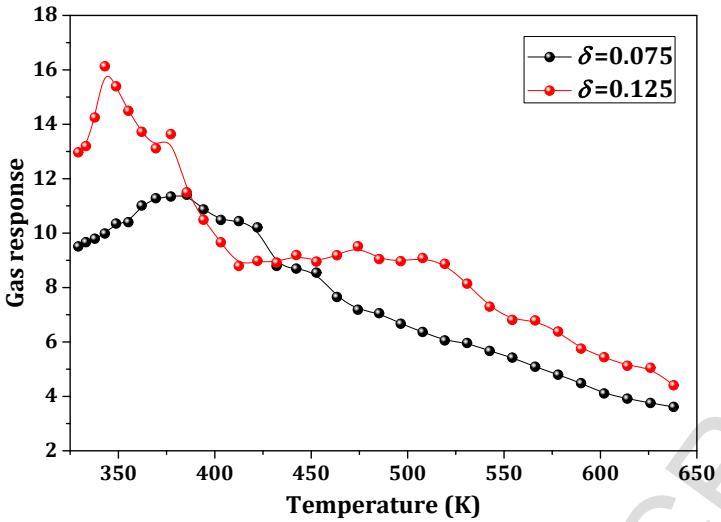

Figure 12: Temperature dependence of the response in ethanol gas of $SrTiO_{3-\delta}$ sensors.

Highlights:

- $SrTiO_{3-\delta}$ (δ=0.075 and 0.125) compounds prepared by the solid state reaction method.

- At room-temperature, $SrTiO_{3-\delta}$ compounds crystallized in cubic symmetry.

- Giant dielectric permittivity (>10^4) was found in $SrTiO_{3-\delta}$ compounds.

- $SrTiO_{3-\delta}$ sensors are *p*-type semiconductor gas-sensing materials.

- Large number of oxygen vacancy enhances the ethanol gas sensitivity.